Check for updates

DFT calculations for single-atom confinement effects of noble metals on monolayer g-C₃N₄ for photocatalytic applications†

Cheng Yang,[ab] Zong-Yan Zhao,*[c] Hai-Tang Wei,[a] Xi-Yu Deng[a] and Qing-Ju Liu [iD] *[a]

Graphitic carbon nitride, as a very promising two-dimensional structure host for single atom catalysts (SACs), has been studied extensively due to its significant confinement effects of single atoms for photocatalytic applications. In this work, a systematic investigation of g-C₃N₄ confining noble metal single atoms (NM₁@g-C₃N₄) will be performed by using DFT calculations. The geometric structure calculations indicate that the most favorable anchored sites for the NM₁ is located in the six-fold cavity, and the deformed wrinkle space of g-C₃N₄ helps the NM₁ to be stabilized in the six-fold cavity. The electronic structure calculations show that the conduction band of NM₁@g-C₃N₄ moved down and crossed through the Fermi level, resulting in narrowing the band gap of the NM₁@g-C₃N₄. Moreover, the confined NM₁ provide a new channel of charge transport between adjacent heptazine units, resulting in a longer lifetime of photo-generated carriers except Ru, Rh, Os and Ir atoms. Furthermore, the d-band centres of NM₁ in NM₁@g-C₃N₄ show that Rh₁@, Pd₁@, Ir₁@ and Pt₁@g-C₃N₄ SACs may have better photocatalytic performance than other NM₁@g-C₃N₄ SACs. Finally, Pt₁@g-C₃N₄ SACs are considered to have higher photocatalytic activity than other NM₁@g-C₃N₄ SACs. These results demonstrate that the confinement effects of noble metals on monolayer g-C₃N₄ not only makes the single atom more stable to be anchored on g-C₃N₄, but also enhances the photocatalytic activity of the system through the synergistic effect between the confined NM₁ and the monolayer g-C₃N₄. These detailed research may provide theoretical support for engineers to prepare photocatalysts with higher activity.

1. Introduction

Environmental pollution and the energy crisis caused by excessive use of fossil fuels are the two major problems that have seriously affected the sustainable development of human being in the world today. Catalytic technologies play a critical role in solving two above-mentioned problems, which have been extensively used in many fields, such as chemical industry, production,[1,2] clean energy technologies[3,4] and environmental treatment.[5,6] Traditional supported metal catalysts, especially noble metals, including ruthenium (Ru), rhodium (Rh), palladium (Pd), silver (Ag), osmium (Os), iridium (Ir), platinum (Pt), gold (Au), have excellent catalytic performance. Therefore, they

are applied in a wide range of heterogeneous catalysis fields.[7–10] As is well-known, heterogeneous catalysts have the advantages of a stable structure and easy separation of products. Meanwhile, they also have some weakness, such as the low metal utilization rate and the low catalyst efficiency, which leads to the wasting of noble metal resources, the increase of production costs and the catalysts to be bulky and heavy. In contrast, homogeneous catalysts have a large number of homogeneous single active sites, which make the catalysts show high catalytic activity and selectivity. However, low stability and difficult separation of products is homogeneous catalysts' Achilles heel. Fortunately, single-atom catalysts (SACs) that were first put forward by Zhang's group in 2011 (ref. 11) are provided with both advantages of heterogeneous and homogeneous catalysts and become the bridge and tie to link both up.[12–14] For the past few years, SACs with the unique electronic structure and unsaturated coordination environment have drawn extensive attention around the world and can be used effectively in many catalytic reactions due to their low noble metal loadings and high utilization rates of noble metal atoms.[15–17] Unfortunately, the specific surface area of noble metal particles increases dramatically with the decrease of the size of noble metal particles to single atom, resulting in a sharp increase in the free energy of the noble metal surface.[18] That is, it is very easy for

[a]School of Materials and Energy, National Center for International Research on Photoelectric and Energy Materials, Yunnan Key Laboratory for Micro/Nano Materials & Technology, Yunnan University, Kunming 650091, P. R. China. E-mail: qjliu@ynu.edu.cn; Fax: +86-871-65032713; Tel: +86-871-65032713

[b]School of Optoelectronic and Communication Engineering, Yunnan Open University, Kunming 650223, P. R. China

[c]Faculty of Materials Science and Engineering, Kunming University of Science and Technology, Kunming 650093, P. R. China. E-mail: zzy@kmust.edu.cn; Fax: +86-871-65107922; Tel: +86-871-65109952

† Electronic supplementary information (ESI) available. See DOI: 10.1039/d0ra09815a

agglomeration to form large particles during the preparation of the catalysts and the catalytic reaction, resulting in deactivation of the catalysts. Therefore, it is very important for SACs to search the suitable confinement supports to effectively confine single atom.[19–21] As a matter of fact, confinement supports can effectively increase kinetic stabilization of a single atom to prevent the aggregation and create well-dispersed SACs by the strong metal–support interactions. Most importantly, confinement supports can also form new electronic structures and new coordination environment to affect the catalytic activity and selectivity.[22] This phenomenon is known as the confinement effects, which have already aroused enormous interest in catalytic research field. In recent years, many confinement supports for SACs have been widely researched, such as FeO_x,[23] CeO_2,[24] WO_x,[25] Al_2O_3,[26] MnO_2,[27] SiO_2,[28] ThO_2,[29] TiC,[30] Mo_2C,[31] metal–organic frameworks (MOFs),[32] and so on.

Two-dimensional (2D) materials have been extensively studied and used in a variety of applications.[33,34] Comparing with traditional three-dimensional (3D) materials, 2D materials are more suitable to confine noble metal single atoms to construct SACs due to their unique physical and chemical properties,[35] including (1) 2D materials have excellent mechanical strength, high chemical and thermal stability; (2) 2D materials can confine more noble metal single atoms to provide more active sites because of their large surface area; (3) 2D materials can regulate the electronic structure of noble metal single atoms to improve the catalytic performance through synergistic effect;[36,37] (4) the intrinsic catalytic activities of the pristine 2D materials can be triggered by the confined noble metal single atoms;[38–40] (5) the vacant structure on both sides of 2D materials is helpful for the adsorption, diffusion and dissociation of reactants and reaction products.

Graphitic carbon nitride (g-C_3N_4), as an emerging kind of 2D material with layered structure, is a typical synthetic polymer semiconductor composed of sp^2 carbon (C) and sp^2 nitrogen (N) atoms forming π-conjugated system.[41] In fact, g-C_3N_4 can be regarded as a special case of graphene via doping of N atoms. But, unlike N-doped graphene, g-C_3N_4 has more N species and a lot of huge N-coordinating cavities available for confining single atoms. More interestingly, pristine g-C_3N_4, as a very promising photocatalyst in itself,[42] has been widely researched in the field of photocatalysis, including contaminant degradation,[43] hydrogen production[44,45] and carbon dioxide (CO_2) reduction.[46,47] However, the photocatalytic property of pristine g-C_3N_4 has been limited due to its serious recombination of photo-generated carriers and narrow light absorption range.[42] Thus, to promote the photocatalytic performance of pristine g-C_3N_4, some SACs photocatalysts via g-C_3N_4 confining noble metal single atoms ($NM_1@g$-C_3N_4, NM = Ru, Rh, Pd, Ag, Os, Ir, Pt, Au) have been researched in recent years. For instance, Gao and co-workers demonstrated that the single atoms of Pd and Pt supported on g-C_3N_4 as an efficient photocatalyst significantly increase catalysts' ability to absorb visible-light and effectively reduce the reaction barriers during CO_2 reduction.[48] Density functional theory (DFT) calculations showed that the preferred product is HCOOH and CH_4 on Pd@g-C_3N_4 SACs and Pt@g-C_3N_4 SACs from CO_2 reduction, respectively. Moreover, Xiong

et al. demonstrated that the charge transfer between confined Pt single atoms and ligand g-C_3N_4 has great effect on photocatalytic reactions. Compared with pristine g-C_3N_4, Pt^{2+} single atoms confined in g-C_3N_4 as catalyst showed higher photocatalytic activity due to its novel electronic structure.[49] Further, Su and co-workers reported that high-valence Pt^{II} ingle atoms confined in g-C_3N_4 can modulate the valence band structure and lower the valence band maximum level of the semiconductor catalyst to tune photocatalytic water splitting performance of pristine g-C_3N_4.[50] This work proposed a new way for preparing high efficient photocatalysts by modifying the valence band structure of that. In brief, noble metal single atoms confined in g-C_3N_4 are a very practical and effective way to improve the photocatalytic performance.

Although the above reports have greatly enhanced our understanding on monolayer g-C_3N_4 as the structure hosts for $NM_1@g$-C_3N_4 SACs, a comprehensive understanding of confinement effects on $NM_1@g$-C_3N_4 SACs for photocatalysis is still missing. In this work, based on DFT calculations, a systematic study on $NM_1@g$-C_3N_4 SACs will be conducted for the first time to reveal the single-atom confinement effects of noble metals on g-C_3N_4 for photocatalysis. The results will help in obtaining a better understanding of confinement effects of $NM_1@g$-C_3N_4 SACs and a new clue of designing many novel photocatalysts with high catalytic activity, stability and selectivity.

2. Computational methods

In this work, all calculations were conducted with Cambridge serial total energy package (CASTEP) module based on DFT.[51] The interaction between valence electrons and the ionic core was described by using the ultra-soft pseudo-potential.[52] The form of the Perdew–Burke–Ernzerhof (PBE) functional at the generalized gradient approximation (GGA) level was employed as the exchange–correlation functional.[53] A plane wave basis set were used to describe electron wave functions with the cut-off energy of 500 eV. The empirical correction method (DFT-D) from the scheme of Tkatchenko and Scheffler (TS) was employed to describe the van der Waals interactions.[54] The irreducible brillouin zone was sampled by Monkhorst–Pack k-point meshes of $3 \times 3 \times 1$ and $5 \times 5 \times 1$ during geometry optimization and electronic properties calculations in the reciprocal space, respectively. The lattice parameters and the positions of atoms were relaxed until the maximum force, the maximum stress, the maximum displacement, maximal energy change and the self-consistent field tolerance were less than 0.03 eV $Å^{-1}$, 0.05 GPa, 1×10^{-3} Å, 1×10^{-5} eV per atom and 1×10^{-6} eV per atom, respectively. In this paper, the calculated band gap value of pristine monolayer g-C_3N_4 (1.16 eV) was far less than the experimental result reported previously (2.70 eV) by Wang and his co-worker,[42] due to the well-known limitations of the GGA method in describing the electronic structures of the materials. Furthermore, since g-C_3N_4 is a covalent system, the band gap correction of g-C_3N_4 is failed using the GGA + U method. However, the hybrid approach which can give the correct band gap is not suitable to describe widely the electronic

stricture of g-C$_3$N$_4$ system due to its huge time cost.[55] In this work, although the band gap value of the system is underestimated, the calculated results can still be used to accurately describe the photocatalytic performance of the system.

To study the stability of NM atoms confined in g-C$_3$N$_4$, the binding energy was computed by the following formula.

$$E_b = E_{NM_1@g-C_3N_4} - E_{g-C_3N_4} - E_{NM_1} \qquad (1)$$

where NM is the single atom of Ru, Rh, Pd, Ag, Os, Ir, Pt or Au; $E_{NM_1@g-C_3N_4}$, $E_{g-C_3N_4}$ and E_{NM_1} represent the total energies of the slab NM$_1$@g-C$_3$N$_4$, slab g-C$_3$N$_4$ and a single NM atom, respectively.

3. Results and discussion

3.1. Optimized structure of pristine monolayer g-C$_3$N$_4$

The tri-s-triazine-based (heptazine) g-C$_3$N$_4$ with perfect layered structures was chosen due to its excellent thermal stability among all the allotropes of g-C$_3$N$_4$.[56] The bulk crystal structure of g-C$_3$N$_4$ was optimized based on the calculation parameters provided in Section 2. The calculation results are as follows: $a = b = 7.127$ Å, $c = 6.289$ Å, $\alpha = \beta = 90°$ and $\gamma = 120.001°$, which are very consistent with previous calculation results,[57,58] and indicates that the computational methods are effective and reliable in this paper.

Further, the monolayer g-C$_3$N$_4$ was constructed by cutting the bulk crystal structure of g-C$_3$N$_4$ along the (001) plane. The 2 × 2 × 1 g-C$_3$N$_4$ supercell consisting of 32 N atoms and 24 C atoms were used in this study. Meanwhile, the vacuum space was built to be 15 Å along z direction, which was enough to avoid periodic interactions between repeated slabs. Based on the computational methods provided in Section 2, the slab model of the monolayer g-C$_3$N$_4$ was optimized. The optimized structure of 2 × 2 × 1 g-C$_3$N$_4$ supercell, whose calculated lattice constant was 7.13 Å, as shown in Fig. 1(a). The calculated results were in good agreement with the previous theoretical[59,60] and experimental[61] results. As can be seen in Fig. 1(a), the 2 × 2 × 1 g-C$_3$N$_4$ supercell consists of four heptazine structural motifs (C$_6$N$_7$) that are connected to each other by bridge N atoms

Fig. 2 The possible deposition sites for NM atoms. Position: S$_1$, centre of the six-fold cavity; S$_2$, corner of the six-fold cavity; S$_3$, top of the five-membered ring; S$_4$, top of N atom; S$_5$, top of C atom; S$_6$, top of the six-membered ring; S$_7$, top of three six-membered rings. The balls in gray and blue represent the C and N atoms, repectively.

labelled as N$_3$. Obviously, a large N-coordinating cavity (six-fold cavity) was formed by six unsaturated N atoms of four heptazine structural motifs. In each of these heptazine structural motifs, there were two classes of non-equivalent C atoms and N atoms, respectively, which were labelled as C$_1$, C$_2$, N$_1$ and N$_2$, as shown in Fig. 1(a).

The calculated bond lengths of C$_1$–N$_1$, C$_1$–N$_2$, C$_2$–N$_2$ and C$_2$–N$_3$ are 1.39 Å, 1.33 Å, 1.34 Å and 1.47 Å, respectively, are in good agreement with the results of the published literature.[59,62] Furthermore, it is evident from Fig. 1(b) that the optimized structure of monolayer pristine g-C$_3$N$_4$ is a stable planar configuration.

3.2. Geometric structures of NM single atoms confined in monolayer g-C$_3$N$_4$

In order to find the most favourable adsorption configuration for NM single atoms confined in pristine g-C$_3$N$_4$, all kinds of adsorption sites around the six-fold cavity were considered on the 2 × 2 × 1 g-C$_3$N$_4$ supercell, as shown in Fig. 2. Each NM single atom species was placed at the S$_1$–S$_7$ sites, respectively, forming 56 kinds of NM$_1$@g-C$_3$N$_4$ configurations in total. The binding energies were obtained when these configurations were fully relaxed, as shown in Table 1. As can be seen from this table, the maximum binding energies are −5.42 eV, −4.08 eV,
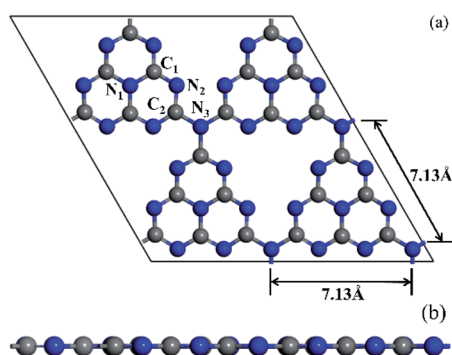

Fig. 1 Top view (a) and side view (b) of optimized structure for 2 × 2 × 1 g-C$_3$N$_4$ supercell. The balls in gray and blue represent the C and N atoms, repectively. Roman numbers labeled on the C and N atoms represent different sites, repectively.
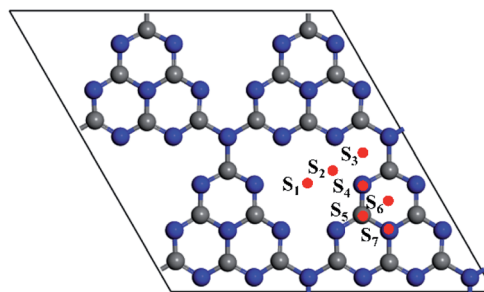
Table 1 The binding energy (E_b) for eight kinds of noble metal atoms at the different adsorption sites

Sites	E_b for NM$_1$@g-C$_3$N$_4$/eV							
	Ru	Rh	Pd	Ag	Os	Ir	Pt	Au
S$_1$	[b]	[b]	[b]	−1.29	−3.28	[b]	[b]	−0.001
S$_2$	−5.42	−4.08	−3.55	[a]	−5.17	−3.57	−3.60	[a]
S$_3$	−4.19	−2.32	[b]	0.12	−3.71	0.65	[b]	0.43
S$_4$	−4.47	−1.89	−0.81	[a]	0.11	1.17	−0.61	0.44
S$_5$	[b]	−0.68	−2.49	0.27	−1.52	0.86	−0.66	0.39
S$_6$	−2.97	0.22	−0.12	0.30	−0.19	1.31	−0.13	0.15
S$_7$	[c]	1.06	−0.45	0.32	1.41	2.55	−0.01	0.43

[a] Moved to S$_1$. [b] Moved to S$_2$. [c] Moved to S$_6$.

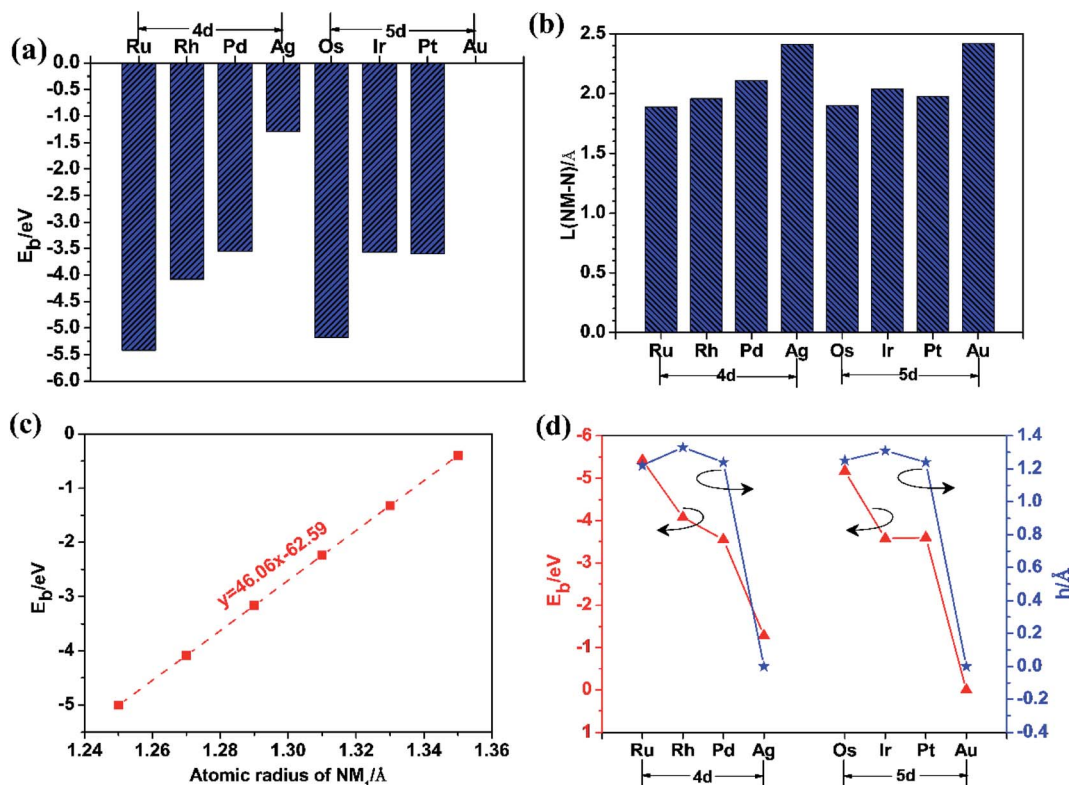© 2021 The Author(s). Published by the Royal Society of Chemistry

Paper

Fig. 3 (a) The binding energy (E_b) of NM_1; (b) the average bond length (L) between NM_1 and N atoms (NM–N); (c) the binding energy (E_b) of NM_1 *versus* the atomic radius of NM_1; (d) the binding energy (E_b) of NM_1 and the geometric deformation (h).

−3.55 eV, −1.29 eV, −5.17 eV, −3.57 eV, −3.60 eV and −0.001 eV for Ru, Rh, Pd, Ag, Os, Ir, Pt and Au single atom at adsorption site S_2, S_2, S_2, S_1, S_2, S_2, S_2, and S_1, respectively. Here, the binding energies were negative, which represented exothermic processes. These results indicate that the site S_2, S_2, S_2, S_1, S_2, S_2, S_2, and S_1 in the six-fold cavity are energetically favourable for Ru, Rh, Pd, Ag, Os, Ir, Pt and Au single atoms confined in g-C_3N_4. However, the Au_1@g-C_3N_4 with positive E_b values ($E_b \approx$ 0 eV for site S_1, 0.15 eV < E_b < 0.44 eV for other sites) at all sites is thermodynamic instability. Therefore, it is difficult for Au single atom to be introduced into the monolayer g-C_3N_4 to prepare Au_1@g-C_3N_4 catalysts. Further, as can be found, the binding energy decreased with increasing atomic number and met 4d > 5d trend, as shown in Fig. 3(a). Meanwhile, the average bond lengths between noble metal atoms and N atoms for eight kinds of noble metal atoms at the different adsorption sites were also obtained, as listed in Table 2. From this table, it had the shortest NM–N bond lengths for eight kinds of noble metal atoms at the site S_1 or S_2 in the six-fold cavity. These sites where the shortest bond lengths occurred correspond exactly to the sites where the maximum binding energies occurred. The results suggest that the shorter the bond length is, the greater the binding energy is. For instance, the Ru–N bond length of 1.89 Å is shortest with a maximum binding energy of −5.42 eV, while the Au–N bond length of 2.42 Å is longest with a minimum binding energy of −0.001 eV. As opposed to the behaviour of the bond lengths and the binding energies, the

bond length increased with increasing atomic number and meets 4d < 5d trend, as shown in Fig. 3(b).

More interestingly, the binding energy for eight kinds of noble metal atoms at the site S_1 or S_2 in the six-fold cavity linearly decreased with increasing atomic radius of NM_1, as shown in Fig. 3(c). This indicates that the larger the atomic radius of NM_1 is, the weaker the confinement effect of the six-fold cavity for NM_1 is. This is because as the radius of NM_1 increase, the confinement configurations become more and more unstable. Moreover, just as shown in Fig. S2 in the ESI,† the introduction of NM_1 resulted in the deformation of pristine

Table 2 The average bond length (L) between NM atoms and N atoms (NM–N) for eight kinds of noble metal atoms at the different adsorption sites

	L(NM–N) for NM@g-C_3N_4/Å							
Sites	Ru	Rh	Pd	Ag	Os	Ir	Pt	Au
S_1	[b]	[b]	[b]	2.41	2.28	[b]	[b]	2.42
S_2	1.89	1.96	2.05	[a]	1.90	2.01	1.98	[a]
S_3	1.97	2.04	[b]	—	1.97	1.99	[b]	—
S_4	1.92	2.05	2.10	[a]	1.91	2.04	2.04	—
S_5	[b]	2.12	2.28	—	1.95	2.09	2.25	—
S_6	2.63	2.23	—	—	2.03	2.19	2.37	—
S_7	[c]	2.01	2.10	—	1.99	2.04	2.00	—

[a] Moved to S1. [b] Moved to S2. [c] Moved to S6.

g-C_3N_4 from a flat shape to a wrinkled shape. This deformation can be characterized on the basis of the thickness (h) of the slab NM_1@g-C_3N_4 SACs, as Fig. 3(d) and S2 in the ESI.† Even more importantly, as shown in Fig. 3(d), the deformation quantity (h) and the binding energy decreased with increasing atomic number, and followed the same variation trend on 4d and 5d. The results indicate that the larger the deformation is in each period, the larger the binding energy is; on the contrary, the smaller the deformation is, the smaller the binding strength is. This may be due to the fact that the single atoms are more easily anchored in the deformed wrinkle space than in the flat structure of g-C_3N_4. The deformed wrinkle space provided an extremely important confined environment for the single atoms. In other words, these results confirm the importance of wrinkle for NM_1@g-C_3N_4 SACs.

In brief, it can be suggested from the above analysis of energy and spatial configuration that the most favourable adsorption sites are S_2, S_2, S_2, S_1, S_2, S_2, S_2, and S_1 for single Ru, Rh, Pd, Ag, Os, Ir, Pt and Au atom confined in pristine g-C_3N_4 catalysts, respectively. In other words, the most favourable confined sites for NM single atoms are located in the six-fold cavity, while Au single atom was hard to confine in g-C_3N_4 due to its small binding energy in the monolayer g-C_3N_4. Moreover, in order to clearly show the most favourable confined configurations of

NM_1@g-C_3N_4, the corresponding top view and side view of that are displayed in Fig. S1 and S2 in the ESI,† respectively.

3.3. Electronic structures of NM single atoms confined in monolayer g-C_3N_4

3.3.1. Density of states. The calculated density of states (DOS) for pristine monolayer g-C_3N_4 and NM_1@g-C_3N_4 are illustrated in Fig. 4. For pristine monolayer g-C_3N_4, it can be seen from Fig. 4(a) that the pristine monolayer g-C_3N_4 exhibits semiconductor characteristics, which are in good agreement with the previous reports.[63] Meanwhile, from Fig. 4(a), it is found that the valance band (VB) is composed mostly of the N_2 atoms around the Fermi level, while the conduction band (CB) edge is mainly made up of the C_1, C_2 atoms and a few of N_1 and N_2 atoms. Also, most remarkably, almost no electrons on either VB or CB around the Fermi level were donated by N_3 atoms, as shown in Fig. 4(a). In order to understand the above conclusions more intuitively and recognize active sites of the pristine monolayer g-C_3N_4 more clearly, the corresponding highest occupied molecular orbital (HOMO) and lowest unoccupied molecular orbital (LUMO) of valence band maximum (VBM) and conduction band minimum (CBM) of the pristine monolayer g-C_3N_4 was obtained, as shown in Fig. 5(a-1) and (b-1). The HOMO and LUMO obtained is consistent with the DOS results
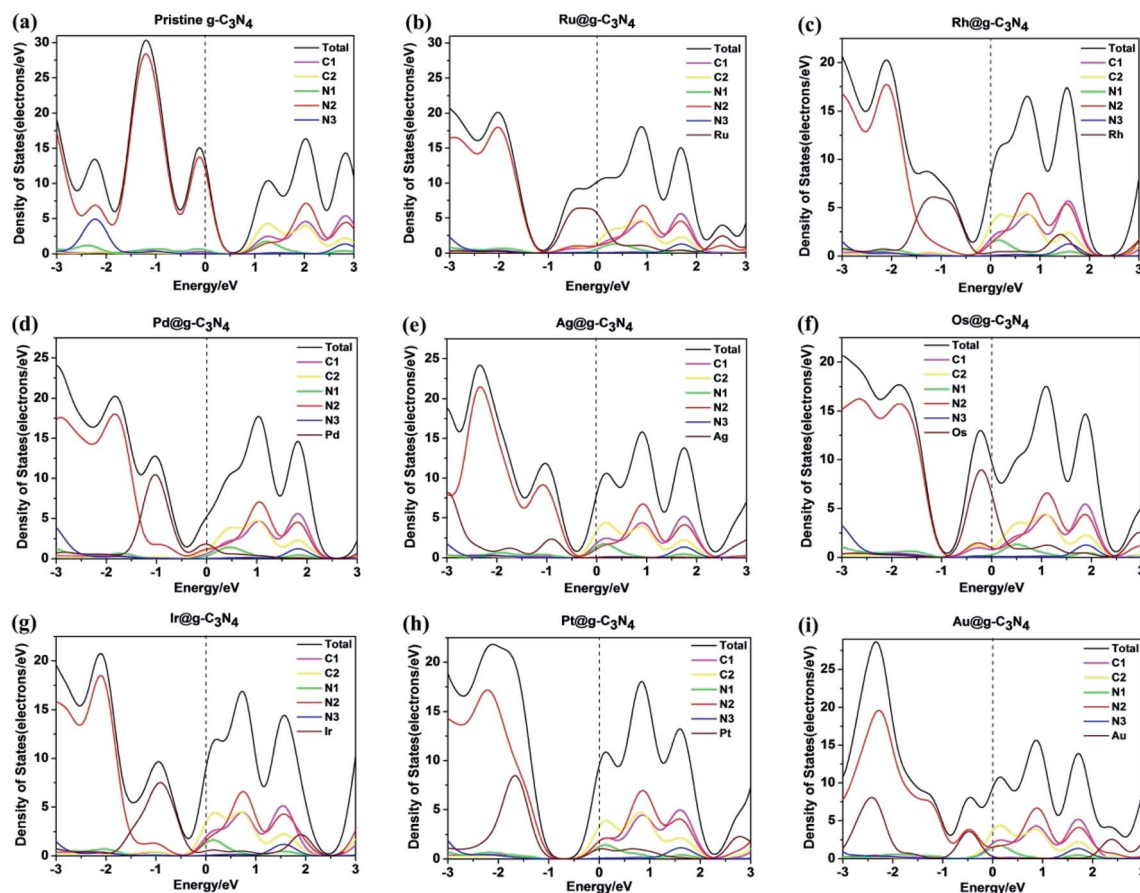

Fig. 4 Density of states for (a) pristine g-C_3N_4 and NM_1@g-C_3N_4, NM_1 = (b) Ru_1, (c) Rh_1, (d) Pd_1, (e) Ag_1, (f) Os_1, (g) Ir_1, (h) Pt_1, (i) Au_1. The Fermi energy is set to zero.
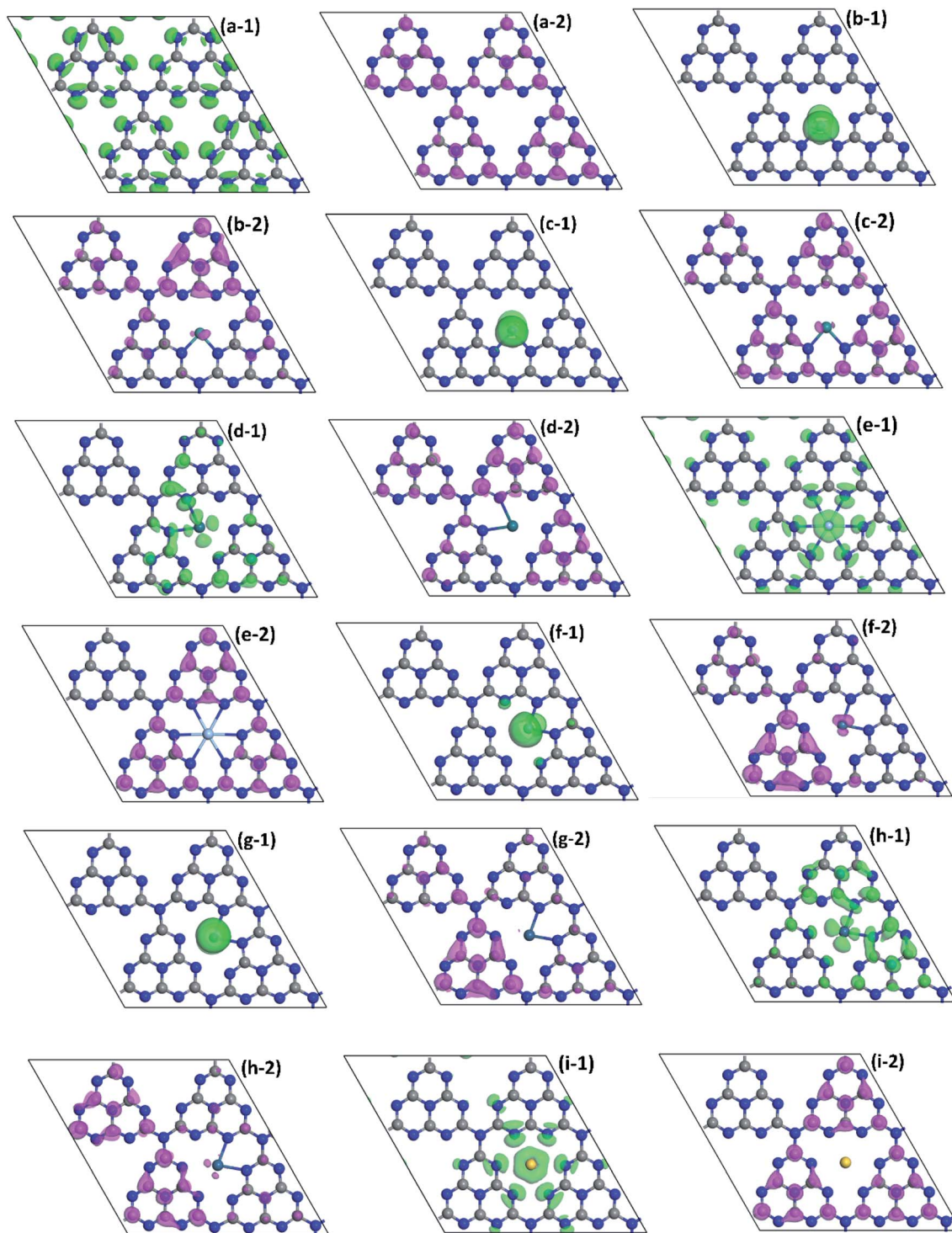
Fig. 5 HOMO (green part) of (a-1) pristine g-C$_3$N$_4$ and NM$_1$@g-C$_3$N$_4$, NM$_1$ = (b-1) Ru$_1$, (c-1) Rh$_1$, (d-1) Pd$_1$, (e-1) Ag$_1$, (f-1) Os$_1$, (g-1) Ir$_1$, (h-1) Pt$_1$, (i-1) Au$_1$; LUMO (purple part) of (a-2) pristine g-C$_3$N$_4$ and NM$_1$@g-C$_3$N$_4$, NM$_1$ = (b-2) Ru$_1$, (c-2) Rh$_1$, (d-2) Pd$_1$, (e-2) Ag$_1$, (f-2) Os$_1$, (g-2) Ir$_1$, (h-2) Pt$_1$, (i-2) Au$_1$. The isovalue is set as 0.05 e Å^{-3}. The balls in gray and blue represent the C and N atoms, repectively.

mentioned above. From Fig. 5(a-1) and (b-1), the HOMO was only found on N$_2$ atoms around the six-fold cavity, while the LUMO was found on C$_1$, C$_2$, and N$_1$ atoms adjacent to N$_2$ atoms in every heptazine unit. The results indicate that N$_2$ atoms exhibit oxidation activities while C$_1$, C$_2$ and N$_1$ atoms exhibit

reduction activities in a photocatalytic reaction, which are consistent with previous reports.[60] Meanwhile, it can be concluded that those localized distributions of the HOMO and the LUMO can lead to low separation efficiency of photo-induced electron–hole pairs. In addition, it is noted that the

bridge N_3 atoms are not covered by either the HOMO or the LUMO. The results show that the electrons cannot be excited and transferred on and by the N_3 atoms under visible-light irradiation. The bridge N_3 atoms only play the role of connecting three adjacent heptazine units instead of acting as a charge transmission channel. In other word, the photo-induced carriers are completely localized in each isolated heptazine unit, resulting in the outstanding recombination of photo-induced carriers and low photocatalytic activity of the pristine monolayer g-C_3N_4.

As shown in Fig. 4(b)–(i), after introducing noble metal single atoms into the monolayer g-C_3N_4, the DOS of NM_1@g-C_3N_4 had been changed greatly compared with that of the pristine g-C_3N_4 in Fig. 4(a). For all NM_1@g-C_3N_4 systems, noble metal single atoms participated mainly in the constitution of VB, while the compositions of CB were almost unchanged compared with the pristine g-C_3N_4. Significantly, only a handful of noble metal single atoms participated in the constitution of CB. In particular, as for Ru_1@, Rh_1@, Pd_1@, Os_1@ and Ir_1@g-C_3N_4, the VB is contributed by noble metal single atoms and a few of N_2 atoms. As regards Ag_1@, Pt_1@ and Au_1@g-C_3N_4, the VB is contributed by the N_2 atoms and a part of noble metal single atoms. Most remarkably, the CB moved down and passed through the Fermi level due to the introduction of noble metal single atoms, resulting in narrowing the band gap of the NM_1@g-C_3N_4 systems. This will effectively improve the visible light response of the systems.

Similarly, to better understand the structure of band edges, the corresponding HOMO and LUMO of VBM and CBM of monolayer NM_1@g-C_3N_4 are shown in Fig. 5(b)–(i). As can be seen from these figures, the HOMO and LUMO of all the monolayer NM_1@g-C_3N_4 had been redistributed compared to that of pristine monolayer g-C_3N_4 in Fig. 5(a). The redistribution of HOMO and LUMO resulted in the variation of the active sites. Meanwhile, the separation of the HOMO and LUMO can effectively promote the photocatalytic performance of 2D materials. More specifically, the distributions of the HOMO and LUMO can be roughly divided into four categories. For monolayer Ru_1@, Rh_1@, Os_1@ and Ir_1@g-C_3N_4, the HOMO mainly covered the noble metal single atoms, while the LUMO covered almost all triazine units except the N_2 and N_3 atoms. In this case, the non-localized distribution of the HOMO and LUMO can effectively promote the separation of photo-generated electron–hole pairs. Photo-generated carriers, however, cannot move freely in adjacent heptazine units because there is neither the HOMO nor the LUMO on the N_3 atoms and the N_2 atoms next to the noble metal single atoms, resulting in short carrier lifetime and poor photocatalytic activity. For monolayer Ag_1@ and Au_1@g-C_3N_4, the HOMO is distributed on the noble metal single atoms and the N_2 atoms, while the LUMO is located on three adjacent heptazine units around Ag and Au single atoms except the N_2 atoms. In this instance, the distribution of the HOMO and LUMO are localized mainly in Ag and Au atoms and three adjacent heptazine units around them. From Fig. 5(e) and (i), after introducing Ag and Au single atoms, photo-generated carriers can be transported through Ag and Au single atom channels among three adjacent heptazine units under visible-

light irradiation. Thus, the introduction of Ag and Au single atoms will enhance the carrier mobility on g-C_3N_4 to some extent. For Pd_1@g-C_3N_4, the HOMO mainly covered on the noble metal single atom and two adjacent heptazine units including it, while the LUMO covered almost all triazine units except Au single atoms, the N_2 and N_3 atoms. For Pt_1@g-C_3N_4, the distributions of the HOMO are similar to that of Pd_1@g-C_3N_4, while the LUMO is distributed on two heptazine units that is not adjacent to Au single atoms. Obviously, for Pd_1@g-C_3N_4 and Pt_1@g-C_3N_4, because of the remarkable delocalized distribution of the HOMO and LUMO, photo-generated electron–hole pairs can be effectively separated. And more notably, as can been found clearly from Fig. 5(d-1) and (h-1), the HOMO is distributed on the N_2 atoms next to Pd and Pt atoms. Therefore, it is reasonable to believe that photo-generated carriers can be transported freely between two adjacent heptazine units through the channels formed by C–N–Pd–N–C or C–N–Pt–N–C chains. This will effectively prolong the carrier lifetime and reduce the recombination rate of photo-generated electron–hole pairs, resulting in high photocatalytic activity. These results are in good agreement with the DOS analysis. In a word, based on the above discussions, it can be inferred that Pd_1@, Pt_1@, Ag_1@ and Au_1@g-C_3N_4 may have better photocatalytic activity than Ru_1@, Rh_1@, Os_1@ and Ir_1@g-C_3N_4.

3.3.2. The d-band centres of NM_1 in NM_1@g-C_3N_4 SACs.

As an effective evaluation parameter, the d-band centre of noble metal single atoms in NM_1@g-C_3N_4 SACs can be used to semi-quantitatively estimate the photocatalytic activities of photo-catalysts.[64,65] This was because the $\sigma \rightarrow$ d interaction and the d $\rightarrow \pi$ interaction between the d-band of metals and the adsorbates (for example, CO, CO_2, H^+ and so on) directly affect the binding strength between noble metal single atoms and the adsorbates. The d-band centre is expressed as follows

$$E_d = \varepsilon_d + \frac{\int_{-\infty}^{+\infty} (x - \varepsilon_d)\rho(x)dx}{2\int_{-\infty}^{\boxplus\infty} \rho(x)dx} \quad (2)$$

where

$$\varepsilon_d = \frac{\int_{-\infty}^{+\infty} x\rho(x)dx}{\int_{-\infty}^{+\infty} \rho(x)dx} \quad (3)$$

The d-band centres of noble metal single atoms in NM_1@g-C_3N_4 SACs are shown in Fig. 6. As we know, the d-band centres
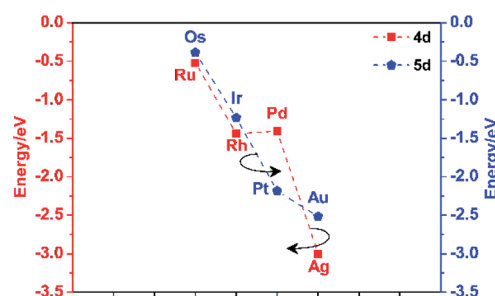

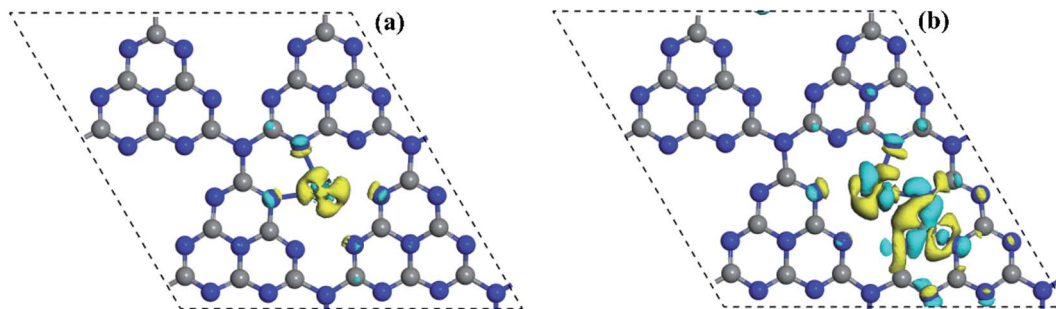**Fig. 6** The d-band centres of noble metal single atoms in NM_1@g-C_3N_4 SACs.

Fig. 7 Plots of 3D charge density difference of (a) $Pd_1@g-C_3N_4$ and (b) $Pt_1@g-C_3N_4$ at isosurfaces of ±0.05 e $Å^{-3}$. The blue and yellow colours represent charge accumulation and depletion, respectively. The balls in gray and blue represent the C and N atoms, repectively.

cannot be too large or too small, otherwise it will not match well with the energy levels of the adsorbates. As can be seen from Fig. 6, the d-band centres show similar change tendency for 4d and 5d noble metals. And, the energy curves for 4d and 5d noble metals cross near the d-band centres of $Rh_1@$, $Pd_1@$, $Ir_1@$ and $Pt_1@g-C_3N_4$ SACs. Meanwhile, the d-band centres of $Rh_1@$, $Pd_1@$, $Ir_1@$ and $Pt_1@g-C_3N_4$ SACs are located in the middle, while the other d-band centres are either too large or too small. In other words, the energy levels matching between $Rh_1@$, $Pd_1@$, $Ir_1@$ and $Pt_1@g-C_3N_4$ SACs and the adsorbates are better than that between $Ru_1@$, $Ag_1@$, $Os_1@$ and $Au_1@g-C_3N_4$ SACs and the adsorbates. Therefore, it can be predicted that $Rh_1@$, $Pd_1@$, $Ir_1@$ and $Pt_1@g-C_3N_4$ SACs may have better photocatalytic performance than $Ru_1@$, $Ag_1@$, $Os_1@$ and $Au_1@g-C_3N_4$ SACs.

Combined with the above discussions, it is reasonable to believe that $Pd_1@g-C_3N_4$ and $Pt_1@g-C_3N_4$ SACs may have more excellent photocatalytic activity than the other $NM_1@g-C_3N_4$ (NM = Ru, Rh, Ag, Os, Ir, Au) SACs.

3.3.3. Differential charge density and Mulliken population analysis. In order to further study the catalytic activity of $Pd_1@g-C_3N_4$ and $Pt_1@g-C_3N_4$ SACs, the 3D differential charge densities of that are shown in Fig. 7. As can be seen from the figure, the charge depletion (the yellow colour) occurred mainly on Pd single atom in $Pd_1@g-C_3N_4$ in Fig. 7(a), while the charge accumulation (the blue colour) and depletion occurred simultaneously on Pt single atom in $Pt_1@g-C_3N_4$ in Fig. 7(b), which indicate that the charge transfer existed between noble metal

single atoms and the N_2 atoms, resulting in strong interaction between noble metal single atoms and the N_2 atoms. Further, in order to describe quantitatively the charge transfer, Mulliken charges were calculated, as listed in Table 3. As can be seen from Table 3, the oxidation states of Pd and Pt single atom are +0.44 and +0.31, respectively. Recent studies suggest that it is very important for the charge transfer between transition metal atoms and $g-C_3N_4$ during catalytic process.[66] In general, the transition metal atoms that can maintain a lower valence states have a stronger ability to capture the adsorbates, resulting in their higher photocatalytic activity.[67] Hence, $Pt_1@g-C_3N_4$ SACs may have higher photocatalytic activity than $Pd_1@g-C_3N_4$ SACs. Moreover, it can be seen from Table 3 that the bond populations of Pd and Pt single atom were 0.18 and 0.25, respectively, indicating that the interaction between Pt single atom and $g-C_3N_4$ is greater than that between Pd single atom and $g-C_3N_4$ due to the stronger covalent bonds between Pt single atom and the N_2 atoms. This result is consistent with the result that the binding energy of Pt single atom (-3.60 eV) is greater than that of Pd single atom (-3.55 eV) in Table 1, and the result that the Pt–N bond length (1.98 Å) is less than the Pd–N bond length (2.05 Å) in Table 2.

In brief, based on all the above discussion, it is reasonable to believe that $Pt_1@g-C_3N_4$ SACs may have higher photocatalytic activity than the other $NM_1@g-C_3N_4$ SACs under the same conditions, and can be considered as one of the most promising $NM_1@g-C_3N_4$ SACs.

4. Conclusions

In summary, the geometric structures and electronic structures of pristine monolayer $g-C_3N_4$ and eight types SACs of the noble metal single atom confined in $g-C_3N_4$ were studied systematically by using DFT calculations. The calculation results of the geometric structures show that the most favourable confined sites for NM single atoms are located in the six-fold cavity. Remarkably, Au single atom is difficult to be confine in $g-C_3N_4$ due to its small binding energy. At the same time, the deformed wrinkle space of $g-C_3N_4$ contributed to the stability of the noble metal single atom in the six-fold cavity of $g-C_3N_4$. The "confining" not only means that the noble metal single atom is constrained by the coordination environment of $g-C_3N_4$, but

Table 3 Mulliken charges and the bond population of noble metal single atoms in the six-fold cavity of $g-C_3N_4$. The unit of Mulliken charge is "e"

Species	Mulliken charges	Bond population
Ru	+0.71	0.23
Rh	+0.69	0.25
Pd	+0.44	0.18
Ag	+0.31	0
Os	+0.60	0.34
Ir	+0.52	0.33
Pt	+0.31	0.25
Au	+0.25	0.01

also means that new electronic state are formed due to the strong electron interaction between the noble metal single atom and g-C_3N_4, so as to realize the modulation of the photocatalytic activity. After introducing the confined noble metal single atoms into the monolayer g-C_3N_4, the CB of the systems moved down and crossed through the Fermi level, causing the band gap of the NM_1@g-C_3N_4 systems to be narrowed, thus increasing its response to visible light. Meanwhile, photogenerated electron–hole pairs can be effectively separated for NM_1@g-C_3N_4 due to the remarkable delocalized distribution of the HOMO and LUMO. Moreover, after introducing the confined Ag and Au single atoms, photo-generated carriers can be transported through Ag and Au single atom channels among three adjacent heptazine units under visible-light irradiation. And, for Pd_1@g-C_3N_4 and Pt_1@g-C_3N_4 SACs, photo-generated carriers can be transported freely between two adjacent heptazine units through the channels formed by C–N–Pd–N–C or C–N–Pt–N–C chains, thus prolonging the lifetime of photo-generated carriers. Especially, Pt_1@g-C_3N_4 single-atom catalysts are considered to have higher photocatalytic activity than the other NM_1@g-C_3N_4 single-atom catalysts. These results provide a new insight into understand single-atom confinement effects of noble metals on monolayer g-C_3N_4 for photocatalytic applications, and a new idea for preparing high-efficiency photocatalysts.

Author contributions

Cheng Yang: investigation, data curation, writing-original draft; Zong-Yan Zhao: methodology, software; Qing-Ju Liu: supervision, conceptualization, methodology, software.

Conflicts of interest

There are no conflicts to declare.

Acknowledgements

Notes and references

1 P. M. Yeletsky, O. O. Zaikina, G. A. Sosnin, R. G. Kukushkin and V. A. Yakovlev, *Fuel Process. Technol.*, 2020, **199**, 106239.

2 J. Ren, J.-P. Cao, F.-L. Yang, X.-Y. Zhao, W. Tang, X. Cui, Q. Chen and X.-Y. Wei, *Energy Convers. Manage.*, 2019, **183**, 182–192.

3 Y. Zhao, M. Que, J. Chen and C. Yang, *J. Mater. Chem. C*, 2020, **8**, 16258–16281.

4 J. Yu, S. Chang, X. Xu, X. He and C. Zhang, *J. Mater. Chem. C*, 2020, **8**, 8887–8895.

5 X. Liu, L. Zhu, X. Wang and X. Meng, *Environ. Sci. Pollut. Res.*, 2020, **27**, 13590–13598.

6 H. Çağlar Yılmaz, E. Akgeyik, S. Bougarrani, M. El Azzouzi and S. Erdemoğlu, *J. Dispersion Sci. Technol.*, 2020, **41**, 414–425.

7 K. Ding, A. Gulec, A. M. Johnson, N. M. Schweitzer, G. D. Stucky, L. D. Marks and P. C. Stair, *Science*, 2015, **350**, 189.

8 R. Lu, L. He, Y. Wang, X.-Q. Gao and W.-C. Li, *Chin. J. Catal.*, 2020, **41**, 350–356.

9 J.-H. Wu, F.-Q. Shao, X.-Q. Luo, H.-J. Xu and A.-J. Wang, *Appl. Surf. Sci.*, 2019, **471**, 935–942.

10 K. Negi, A. Umar, M. S. Chauhan and M. S. Akhtar, *Ceram. Int.*, 2019, **45**, 20509–20517.

11 B. Qiao, A. Wang, X. Yang, L. F. Allard, Z. Jiang, Y. Cui, J. Liu, J. Li and T. Zhang, *Nat. Chem.*, 2011, **3**, 634.

12 F. Chen, X. Jiang, L. Zhang, R. Lang and B. Qiao, *Chin. J. Catal.*, 2018, **39**, 893–898.

13 R. Lang, T. Li, D. Matsumura, S. Miao, Y. Ren, Y. Cui, Y. Tan, B. Qiao, L. Li, A. Wang, X. Wang and T. Zhang, *Angew. Chem.*, 2016, 128.

14 P. Liu, Y. Zhao, R. Qin, S. Mo, G. Chen, L. Gu, D. Chevrier, P. Zhang, Q. Guo, D. Zang, B. Wu, G. Fu and N. Zheng, *Science*, 2016, **352**, 797–800.

15 L. Lin, W. Zhou, R. Gao, S. Yao, X. Zhang, W. Xu, S. Zheng, Z. Jiang, Q. Yu, Y.-W. Li, C. Shi, X.-D. Wen and D. Ma, *Nature*, 2017, 544.

16 J. Zhang, X. Wu, W.-C. M. Cheong, W. Chen, R. Lin, J. Li, L. Zheng, W. Yan, L. Gu, C. Chen, Q. Peng, D. Wang and Y. Li, *Nat. Commun.*, 2018, **9**, 1002.

17 G. Liu, A. Robertson, M. Li, W. Kuo, M. Darby, M. Muhieddine, Y.-C. Lin, K. Suenaga, M. Stamatakis, J. Warner and S. Tsang, *Nat. Chem.*, 2017, **9**, 810–816.

18 X.-F. Yang, A. Wang, B. Qiao, J. Li, J. Liu and T. Zhang, *Acc. Chem. Res.*, 2013, **46**, 1740–1748.

19 C. Wang, X.-K. Gu, H. Yan, Y. Lin, L. Junjie, D. Liu, W.-X. Li and J. Lu, *ACS Catal.*, 2017, **7**, 887–891.

20 M. Kale and P. Christopher, *ACS Catal.*, 2016, **6**, 5599–5609.

21 G. X. Pei, X. Y. Liu, X. Yang, L. Zhang, A. Wang, L. Li, H. Wang, X. Wang and T. Zhang, *ACS Catal.*, 2017, 7, 1491–1500.

22 D. Deng, K. Novoselov, Q. Fu, N. Zheng, Z. Tian and X. Bao, *Nat. Nanotechnol.*, 2016, **11**, 218–230.

23 X. Sun, J. Lin, Y. Zhou, L. Li, Y. Su, X. Wang and T. Zhang, *AIChE J.*, 2017, **63**, 4022–4031.

24 N. Daelman, M. Capdevila-Cortada and N. López, *Nat. Mater.*, 2019, **18**, 1215–1221.

25 M. Zhou, M. Yang, X. Yang, X. Zhao, L. Sun, W. Deng, A. Wang, J. Li and T. Zhang, *Chin. J. Catal.*, 2020, **41**, 524–532.

26 T. Len, C. Dessal, F. Morfin, J. L. Rousset, P. Afanasiev and L. Piccolo, *Presented in Part at the 25ièmes journées du Groupe Français de Spectroscopie Vibrationnelle (GFSV), Ecully, France, 2019-05-13*, 2019.

27 H. Zhang, S. Sui, X. Zheng, R. Cao and P. Zhang, *Appl. Catal., B*, 2019, **257**, 117878.

28 R. Huang, Y. Cheng, Y. Ji and R. J. Gorte, *Nanomaterials*, 2020, 10.

29 B. Long, Y. Tang and J. Li, *Nano Res.*, 2016, **9**, 3868–3880.

30 Y. Wang, X. Zhang, C. Cheng and Z. Yang, *Appl. Surf. Sci.*, 2018, **453**, 159–165.

31 Q. Li, Z. Ma, R. Sa, H. Adidharma, K. A. M. Gasem, A. G. Russell, M. Fan and K. Wu, *J. Mater. Chem. A*, 2017, **5**, 14658–14672.

32 H. Zhang, J. Wei, J. Dong, G. Liu, L. Shi, P. An, G. Zhao, J. Kong, X. Wang, X. Meng, J. Zhang and J. Ye, *Angew. Chem., Int. Ed.*, 2016, **55**, 14310–14314.

33 H. Xiong and F. Yang, *Opt. Express*, 2020, **28**, 5306–5316.

34 V. Dutta, P. Singh, P. Shandilya, S. Sharma, P. Raizada, A. K. Saini, V. K. Gupta, A. Hosseini-Bandegharaei, S. Agarwal and A. Rahmani-Sani, *J. Environ. Chem. Eng.*, 2019, **7**, 103132.

35 S. Gao, Y. Lin, X. Jiao, Y. Sun, Q. Luo, W. Zhang, D. Li, J. Yang and Y. Xie, *Nature*, 2016, **529**, 68–71.

36 Y. Wang, Z. Rong, Y. Wang, T. Wang, Q. Du, Y. Wang and J. Qu, *ACS Sustainable Chem. Eng.*, 2017, **5**, 1538–1548.

37 Y. Wang, Z. Rong, Y. Wang and J. Qu, *J. Catal.*, 2016, **333**, 8–16.

38 Y. Tu, P. Ren, D. Deng and X. Bao, *Nano Energy*, 2018, **52**, 494–500.

39 J. Deng, P. Ren, D. Deng and X. Bao, *Angew. Chem., Int. Ed.*, 2015, **54**, 2100–2104.

40 X. Cui, P. Ren, D. Deng, J. Deng and X. Bao, *Energy Environ. Sci.*, 2016, **9**, 123–129.

41 A. Thomas, A. Fischer, F. Goettmann, M. Antonietti, J.-O. Müller, R. Schlögl and J. M. Carlsson, *J. Mater. Chem.*, 2008, **18**, 4893–4908.

42 X. Wang, K. Maeda, A. Thomas, K. Takanabe, G. Xin, J. M. Carlsson, K. Domen and M. Antonietti, *Nat. Mater.*, 2009, **8**, 76–80.

43 T. Xu, D. Wang, L. Dong, H. Shen, W. Lu and W. Chen, *Appl. Catal., B*, 2019, **244**, 96–106.

44 P. Ganguly, M. Harb, Z. Cao, L. Cavallo, A. Breen, S. Dervin, D. D. Dionysiou and S. C. Pillai, *ACS Energy Lett.*, 2019, **4**, 1687–1709.

45 J. Pan, Z. Dong, B. Wang, Z. Jiang, C. Zhao, J. Wang, C. Song, Y. Zheng and C. Li, *Appl. Catal., B*, 2019, **242**, 92–99.

46 Y. Huo, J. Zhang, K. Dai, Q. Li, J. Lv, G. Zhu and C. Liang, *Appl. Catal., B*, 2019, **241**, 528–538.

47 K. Maeda, *Adv. Mater.*, 2019, **31**, 1808205.

48 G. Gao, Y. Jiao, E. R. Waclawik and A. Du, *J. Am. Chem. Soc.*, 2016, **138**, 6292–6297.

49 Y. Li, Z. Wang, T. Xia, H. Ju, K. Zhang, R. Long, Q. Xu, C. Wang, L. Song and J. Zhu, *Adv. Mater.*, 2016, **28**, 6959–6965.

50 H. Su, W. Che, F. Tang, W. Cheng, X. Zhao, H. Zhang and Q. Liu, *J. Phys. Chem. C*, 2018, **122**, 21108–21114.

51 M. Segall, P. J. Lindan, M. Probert, C. Pickard, P. Hasnip, S. Clark and M. Payne, *J. Phys.: Condens. Matter*, 2002, **14**, 2717–2744.

52 D. Vanderbilt, *Phys. Rev. B*, 1990, **41**, 7892–7895.

53 J. P. Perdew, K. Burke and M. Ernzerhof, *Phys. Rev. Lett.*, 1996, **77**, 3865–3868.

54 A. Tkatchenko and M. Scheffler, *Phys. Rev. Lett.*, 2009, **102**, 073005.

55 G. Dong, K. Zhao and L. Zhang, *Chem. Commun.*, 2012, **48**, 6178–6180.

56 E. Kroke, M. Schwarz, E. Horath-Bordon, P. Kroll, B. Noll and A. D. Norman, *New J. Chem.*, 2002, **26**, 508–512.

57 X. G. Ma, Y. H. Lv, J. Xu, Y. F. Liu and Y. F. Zhu, *J. Phys. Chem. C*, 2012, **116**, 23485–23493.

58 H. W. Zuo, C. H. Lu, Y. R. Ren, Y. Li, Y. F. Zhang and W. K. Chen, *Acta Phys.-Chim. Sin.*, 2016, **32**, 1183–1190.

59 B. Zhu, J. Zhang, C. Jiang, B. Cheng and J. Yu, *Appl. Catal., B*, 2017, **207**, 27–34.

60 J. Cui, S. Liang, X. Wang and J. Zhang, *Mater. Chem. Phys.*, 2015, **161**, 194–200.

61 J. B. Michael, J. O. Müller, M. Antonietti and A. Thomas, *Chem.–Eur. J.*, 2008, **14**, 8177–8182.

62 S. M. Aspera, M. David and H. Kasai, *Jpn. J. Appl. Phys.*, 2010, **49**, 115703.

63 X. Jin, R. Wang, L. Zhang, R. Si, M. Shen, M. Wang, J. Tian and J. Shi, *Angew. Chem.*, 2020, **132**, 6894–6898.

64 B. Hammer and J. K. Nørskov, *Surf. Sci.*, 1995, **343**, 211–220.

65 J. Liang, Q. Yu, X. Yang, T. Zhang and J. Li, *Nano Res.*, 2018, **11**, 1599–1611.

66 Q. Liu and J. Zhang, *Langmuir*, 2013, **29**, 3821–3828.

67 C. Liu, B. Yang, E. Tyo, S. Seifert, J. DeBartolo, B. von Issendorff, P. Zapol, S. Vajda and L. A. Curtiss, *J. Am. Chem. Soc.*, 2015, **137**, 8676–8679.